J Mater Sci: Mater Electron **(2025) 36:104**

2-ethylhexylamine additive boosts the transport properties of PVA-based polymer electrolyte for quasi-solid-state magnesium batteries

S. Y. Ibrahim[1], S. Abouelhassan[1], and E. Sheha[1,*]

[1] *Physics Department, Faculty of Science, Benha University, Benha 13518, Egypt*

Received: 8 October 2024
Accepted: 9 December 2024
Published online: 8 January 2025

ABSTRACT

Magnesium-sulfur (Mg-S) batteries offer excellent energy density, safety, and a cost-effective energy storage system. Realizing Mg-S batteries requires bypassing significant challenges like electrolyte compatibility with electrophilic sulfur and Mg metal and polysulfide shuttling. The present work probes the role of 2-ethylhexylamine (EHA) in modifying the physiochemical properties of solid polymer electrolytes (SPEs) based on polyvinyl alcohol (PVA), silicon dioxide (SiO_2), and magnesium triflate (MgTIF). The introduction of EHA increases the conductivity to approximately 10^{-7} S/cm at room temperature, reduces the magnesium stripping/plating overpotential, and improves the interfacial electrode/electrolyte kinetics; further, the optimum concentration ($y = 3000$ µl) of PVST_yEHA shows a high ionic transference number ($t_{mg^{2+}} = 0.88$) (where PVST is an abbreviation for compound composed of (PVA, SiO_2, MgTIF)), there is minimal overpotential over 100 h. Based on optimum concentration ($y = 3000$ µl), the Mg-S battery exhibits a high initial discharge-specific capacity in the first cycle up to 1837 $mAhg^{-1}$, and over six cycles, it maintained a reversible capacity of 376 $mAhg^{-1}$. The present article attempts to overcome some obstacles that prohibit the realization of Mg-S batteries.

1 Introduction

Magnesium-sulfur (Mg-S) batteries are a promising energy storage system due to excellent energy density, safety, and economical electrochemical energy storage[1]. Mg-S batteries contain Mg-anode and sulfur cathode; Mg and S are prevalent in the earth's crust and can be found in mineral byproducts. Combining an Mg-anode, a sulfur cathode, and a powerful electrolyte in Mg-S full cell gives a theoretical energy density of 3221 Wh L^{-1}, surpassing that of Li–S batteries (2856 Wh L^{-1}), due to the two-electron transfers between the S-cathode and Mg-anode, yielding a theoretical voltage of 1.77 V[2–4]. However, the sulfur cathode has an electrophilic nature that can decompose the common electrolytes, and this requires developing and employing non-nucleophilic electrolytes[5, 6]. Solid polymer electrolytes (SPEs) address some of these issues due to their superior mechanical properties, freedom from leakage, electrochemical stability, and safety, and improved ion transport properties compared to liquid electrolytes [7–11].They have high thermal stability

Address correspondence to E-mail: islam.shihah@fsc.bu.edu.eg

and low ionic conductivity compared to liquid electrolytes. PVA is a well-known membrane material with amazing qualities such as good thermal stability, high dielectric constant, chemical stability, hydrophilicity, and great film-forming capability[12–14]. PVA-based polymer electrolytes have been studied as a promising electrolyte system for different energy storage systems[15, 16]; for example, PVA-CN gel polymer electrolyte enhances the cycle and self-discharge performance of Li–S batteries [17]. Combining organic polymers with inorganic oxide filler trailers thermal stability, rigidity, mechanical qualities, and electrical properties of organic polymers. Silica is a perfect inorganic oxide due to its good heat stability, well-defined ordered structure, high mechanical strength, and large specific surface area[18, 19]. PVA_SiO_2 composite nanofiber-based polymer electrolyte shows great electrolyte affinity, good thermal stability, and electrochemical performance for LIBs[12].

The community has created room temperature molten salt-based electrolyte systems with and without chlorine, employing magnesium triflate (MgTIF) as a simple magnesium salt source[20]. MgTIF-based electrolytes have good characteristics such as being thermally stable, low-cost, non-corrosive, and non-nucleophilic with excellent anodization stability and are a good option for producing high-performing Mg-S batteries [20, 21]. MgTIF has been employed to great artificial polymer coatings on magnesium anodes or used directly as solid polymer electrolyte reactants in Mg batteries and expected that MgTIF has improved anode contact stability [22, 23]; for example, the conductivity of the PVA-based gel electrolyte increased with increasing MgTIF concentration, reaching a maximum of 5.41×10^{-4} S·cm^{-1} at room temperature when the concentration reached 40 wt.%[24].

To further improve the SPE has been added 2-ethylhexylamine($C_8H_{19}N$))EHA(, consists of a main C_8 monoalkylamine with a branching carbon backbone and is a useful intermediate with a wide range of applications. The source material of EHA is 2-ethylhexanol, a propene-based oxo alcohol. It is established that EHA pillared vanadium disulfide nanoflowers (VS_2) significantly increased the interlayer spacing for accelerating ion diffusion and protected the electrostatic interaction between magnesium species and the VS_2 host. In addition, as interstitial pillars, the 2-ethylhexylamine molecule intercalants support and protect the host framework's integrity, allowing for long-term discharge/charge cycles[25]. EHA improves over-electrochemical and electron transport properties [26].On the other hand, there are various challenges to improving the S-cathode, including low sulfur utilization, rapid capacity fading, low coulombic efficiency, anode poisoning, and self-discharge issues[27], these difficulties are due to the insulating properties of sulfur and the migration of long-chain lithium polysulfides (LiPs) during cycling. An appropriate cathode material should have high electrical conductivity and affinity for LiPs[27, 28]. Choose created 3D porous SiC materials that retain active sp^2 hybridized Si atoms while allowing for variable porosity-like LiPs in porous carbon, due to nano-confinement. 3D-SiC hosts outperform 2D-SiC nanosheets in S_8 and LiPs trapping. Three-dimensional (3D) porous SiC materials containing active sp^2 hybridized Si atoms have been devised to trap lithium polysulfide in Li–S batteries. Utilizing a 3D porous SiC host may help guide the design of cathode materials for Li–S batteries with improved electrochemical performance[27]. Solid-state polymer batteries still require significant research and manufacturing. There are several viewpoints on solid magnesium-ion electrolytes. Such as artificial solid electrolyte interfacial contact between the electrolyte and the electrode, preparing thin film electrolytes with high Mg ionic conductivity, doping changes to improve the ionic conductivity while decreasing the electric conductivity of solid electrolytes and advanced characterization techniques and machine learning to investigate Mg^{2+} migration pathways and adjust electrolytes[29]. The ionic conductivity of the solid polymer electrolyte must be greater than 10^{-4} S cm^{-1} at room temperature to maintain the battery's consistent charging and discharging behavior. Herein, we are improving the electrolyte and the cathode in the Mg-S batteries. The solid polymer electrolyte (SPE) of PVA, SiO_2, MgTIF, and EHA is prepared by using the casting technique. The structure, optical, and electrochemical properties are studied. A dual polymer electrolyte of (SPE | halogen-free electrolyte (HFE)) is engineered. XRD, SEM, EDS, mapping, and thermal analysis were used to support our results. FTIR and UV–Vis methods were used to examine our results. The electrochemical behavior of electrolytes was examined using electrochemical impedance spectroscopy (EIS), linear sweep voltammetry (LSV), ion transference (IT), and stripping/plating (S.P) for the overpotentials of Mg. This study is among the first of its kind because the combination of EHA with MgTIF has not before been described using PVA as a host.

2 Experimental section

The solid polymer electrolyte (SPE) was prepared by dissolving 2 gm of PVA (QualiKems Chemical Company, India) over 24 h at 70 °C with constant stirring in 20 ml of deionized water. The PVA solution was combined with 2, 4, 6, and 8 $_{wt.\%}$ SiO_2 (Aldrich Chemical Company). The different concentration solutions were directly poured into glass Petri plates and left to dry for five days at 30°C to prepare PVA$_{-xwt.\%}SiO_2$ films(where x is the concentration of SiO_2). Six (PVA-8wt.%SiO2) composite bottles were prepared, and 28% MgTIF was dissolved in each bottle. Then, 1000, 2000, 3000, 4000, and 5000 µL of different concentrations of EHA were separately added to the PVST (these composites were abbreviated as PVST-yEHA, where y is the concentration of EHA), and then mixed for 12 h at 70 °C as shown in Fig. 1. Halogen-free electrolyte (HFE) was synthesized according to reference [25], where $(Mg(NO_3)_2.H_2O$ (Sigma-Aldrich-ACS reagent, 99%) was dried at 80 °C to remove moisture molecules. The resulting solution was then dissolved in a cosolvent of 5.7 ml of acetonitrile (ACN) (C_2H_3N, Fisher 99.9%) and 2.7 ml of tetra ethylene glycol dimethyl ether (G_4) ($C_{10}H_{22}O_5$, sigma-Aldrich ≥ 99%). The cathode was prepared by grinding a mixture of $_{80wt.\%}$sulfur (S, Alfa Aesar99%) with $_{10wt.\%}$silicon carbide (SiC, Qualicum 99%), and $_{10wt.\%}$graphene nanoplatelets (GNPs, Grade M, XG Science), then put the mixture in a ball mill for 24 h. The mixture was dried in the microwave for 10 s. N-methyl-2-pyrrolidinone (C_5H_9NO) was added to $_{75wt.\%}$Mixture with $_{15wt.\%}$polyvinylidenefluoride (PVDF) and $_{10wt.\%}$ super carbon to dissolve, then spread the cathode on aluminum foil (thickness = 0.1 mm) with a thickness of 150 µm using MC-20 Mini-Coater, dry it in the oven at 200 °C for 1 h, and cut it into round discs of 14 mm. Cathode coating separators were prepared by grinding a mixture of $_{60wt.\%}$SiC with $_{30wt.\%}$C and $_{10wt.\%}$PVDF, then putting the mixture in a ball mill for 24 h and adding n-methyl-2-pyrrolidinone (C_5H_9NO) to dissolve the mixture. The Rigaku MiniFlex 600 diffractometer was used to record the XRD pattern. Thermal analysis such as Differential scanning calorimetry (DSC), and Thermogravimetric analysis (TGA) were recorded using the SDT Q600 V20.9 Build 20. Edinburgh DS5 dual beam spectrophotometer was used to get UV–VIS spectral data. An ALPHA II Bruker spectrometer

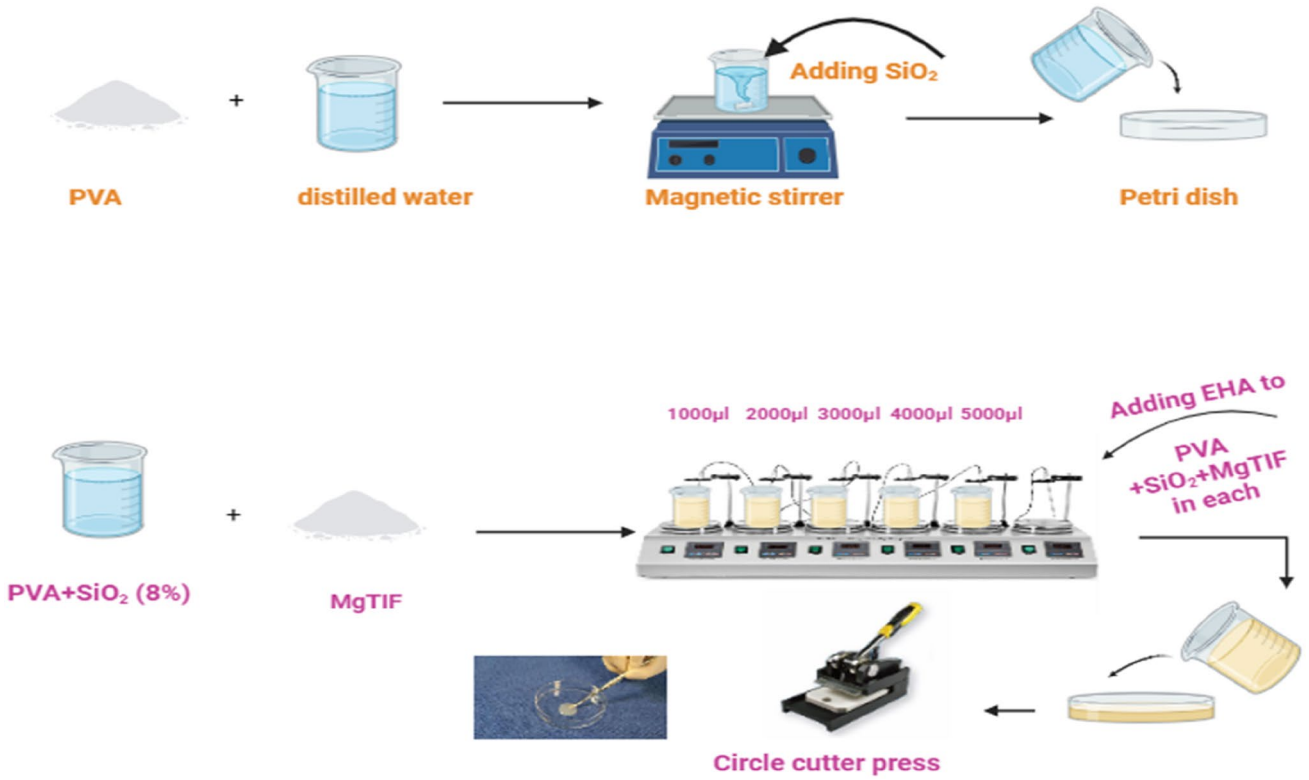

Fig. 1 The preparation of solid polymer electrolyte

performed ATR-FTIR between 400 and 4000 cm^{-1}. SEM images, EDS, and mapping were recorded using a Jeol JMS-700 EDS electron microscope. The SPEs underwent electrochemical testing; the ionic conductivities were determined using a symmetric cell of SS|SPE_EHF|SS cells between 1 MHz and 10 Hz from room temperature to 65 °C was investigated using a CHI605E electrochemical workstation with two electrodes: a working electrode and a counter with a reference electrode of 0.005 V amplitude. Z-View software was used to calculate all the impedance parameters. S.P of Mg|SPE_EHF|Mg half-cell was completed at 25 °C utilizing a NEWARE BTS4000 battery tester with 0.02 mA/cm^2. CHI605E electrochemical workstation was used to perform cyclic voltammetry (CV) of Mg|SPE_EHF|S, IT of Mg|SPE_EHF|Mg cell, and LSV of Mg|SPE_EHF|SS. The NEWARE BTS4000 battery tester was used to measure the (Discharge _ Charge) Mg|SPE_EHF|S. Argon-filled glove box and Cr2332 coin cells were used for all measurements. The cathode discs were extracted after disassembling of Mg|SPE_EHF|S cell and then cleaning using acetonitrile (ACN) and drying to explore the structure and morphology at various electrochemical states using x-ray diffraction (XRD), scanning electron microscopy (SEM), energy-dispersive x-ray spectroscopy (EDS), and mapping.

3 Results and discussions

Figure 2a–c shows the FTIR spectra of $PVA_{\_xwt.\%}SiO_2$; the bands at the wavenumber range 3150–3450 cm^{-1} indicate the O–H stretching vibration of hydroxyl groups. The area under the peak and its intensity decrease with increasing $_{xwt.\%}SiO_2$ [30]. This suggests that some of the hydroxyl groups of PVA participated in a condensation process with silanol groups in silica sol, resulting in covalently bound cross-links between organic groups and silica[30]. The bands at 2924 cm^{-1} represent the stretching vibrations of CH and CH_2 groups, and the bands at 1426 cm^{-1} match with C-H bending vibration within the PVA chains[30, 31]. Additionally, a strong band at 1727 cm^{-1} represents C = O carbonyl functional units in the remaining unreacted acetate groups after the production process in PVA. The bands at 1098 cm^{-1} match the C-O stretching vibration associated with the PVA matrix. The energy band gap E_g that requires the transfer of the electron from the valance band to the conduction band in $PVA_{\_xwt.\%}SiO_2$ composite was calculated using Tauc's relations [32] [33]: $\alpha h\nu = \beta[h\upsilon - E_g]^n$, where $\alpha = 2.303 \frac{A}{t}$ is the absorbance coefficient of incident photon energy, β is the fitting constant, and n is equivalent to half or 2 for direct and indirect transitions from the valence band to the conduction band, respectively. Figure 2d shows the fitting curves of $(\alpha h\nu)^2$ versus hυ of $PVA_{\_xwt.\%}SiO_2$. The value of E_g drops as the ratio of SiO_2 increases as observed in Table 1, which can be attributed to the increase in the localized states in the energy gap and the distribution in the degree of disorder within the PVA matrix [32] [34]. The extinction coefficient $K = \frac{\alpha\lambda}{4\pi}$ represents the amount of absorbing loss as electromagnetic waves pass through the film[33] [35]. Figure 2e shows the K versus λ curve of $PVA_{\_xwt.\%}SiO_2$; it looks like the extinction coefficient decreases sharply in the high photon energy region while increasing simply in the low energy region and further increases with increasing the content of SiO_2 within the PVA matrix.

Generally, the high value of the extinction coefficient demonstrates high dissipation of light energy by scattering, in visible region and upon introduction of SiO_2 [34]. The refractive index $n = \frac{(1+R)}{(1-R)} + \sqrt{\frac{4R}{(1-R)^2} - K^2}$ [32], where R represents reflectance coefficient can be calculated from the relation $A + R + T = 1$, A represents the absorption coefficient, and T represents the transmission coefficient. Figure 2f shows the refractive index (n) versus wavelength (λ) curves of $PVA_{\_xwt.\%}SiO_2$ composite; the value of n decreases with increasing λ, while it increases with increasing the ratio of SiO_2, which can be attributed to changes in hydrogen bonding's interatomic distance of the PVA matrix[32]. Figure 3a shows the heat flow versus temperature of $PVA_{\_xwt.\%}SiO_2$ composite, the value of glass transition temperature T_g for pure PVA equals 49 °C. Adding SiO_2 to PVA increases T_g; however, when the $_{xwt.\%}SiO_2$ increases, T_g cannot be observed because all PVA chains are crosslinked with SiO_2 and are difficult to move[36]. Figure 3b shows the weight loss versus temperature of $PVA_{\_xwt.\%}SiO_2$ composite; the thermal degradation of pure PVA are three weight loss steps. The first, second, and third steps started at ā 76 °C, 216 °C, and 400 °C, respectively, which can be attributed to the removal of the absorbed water from the PVA matrix, the disposal of the side groups of PVA, and the decomposition of the main

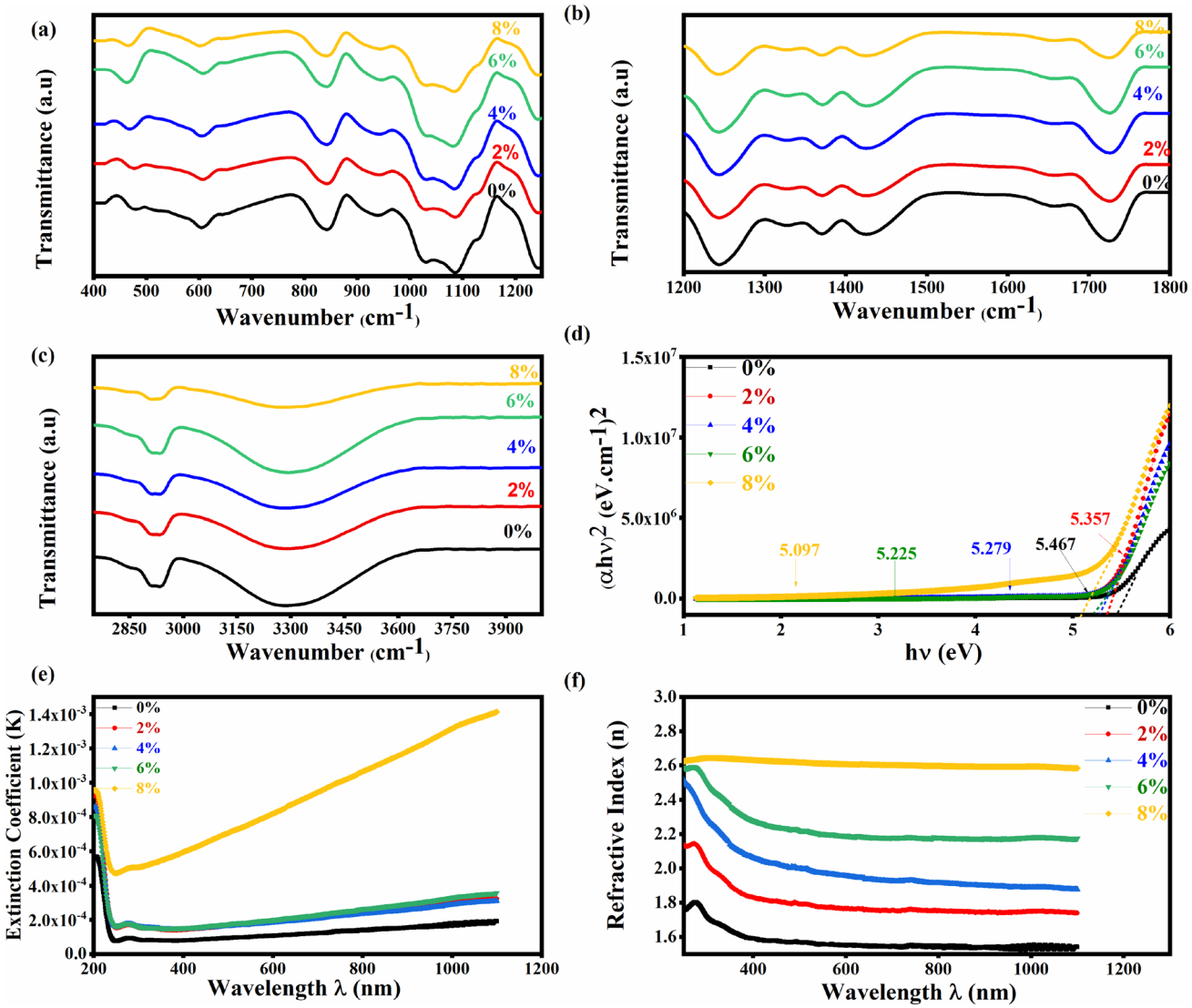

Fig. 2 FTIR spectra of PVA_xwt.%SiO_2 at different wavelength ranges **a** 400 to 1200 cm^{-1}; **b** 1200 to1800 cm^{-1}; **c** 2750–4000 cm^{-1}; **d** Tauc's plot; **e** Extinction coefficient K versus wavelength λ; **f** Refractive index n versus wavelength λ of PVA_xwt.%SiO_2

Table 1 The E_g values of PVA_xwt.%SiO_2 composite

Samples (wt.%)	E_g(eV)
0	5.467
2	5.357
4	5.297
6	5.225
8	5.097

chain of PVA, respectively [37–39]. The introduction of SiO_2 leads to a shifted degradation temperature to the higher and improvement in thermal stability; because SiO_2 acts as heat insulation[31]. The thermal parameters are important in developing efficient functional materials and determining the thermal activation energy E_{at} by means of Coates and Redfern's integral equation [40, 41]: $\log[\frac{1-(1-\alpha)}{T^2}] = \log\left[\frac{R}{\Delta E_a}\left(1-\frac{2RT}{E_{at}}\right)\right] - 0.434\frac{E_{at}}{RT}$, where α is weight loss $= \frac{w_i-w_a}{w_i-w_f}$, w_i, w_a and w_f are the initial, actual, and final sample weights, respectively, T is absolute temperature, and R is the universal gas constant.

Figure 3c shows $-\log\{-\log[\frac{1-(1-\alpha)}{T^2}]\}$ versus $\frac{1000}{T}$ curves of PVA_xwt.%SiO_2 composite, and E_{at} is determined from the slope and listed in Table 2 which can

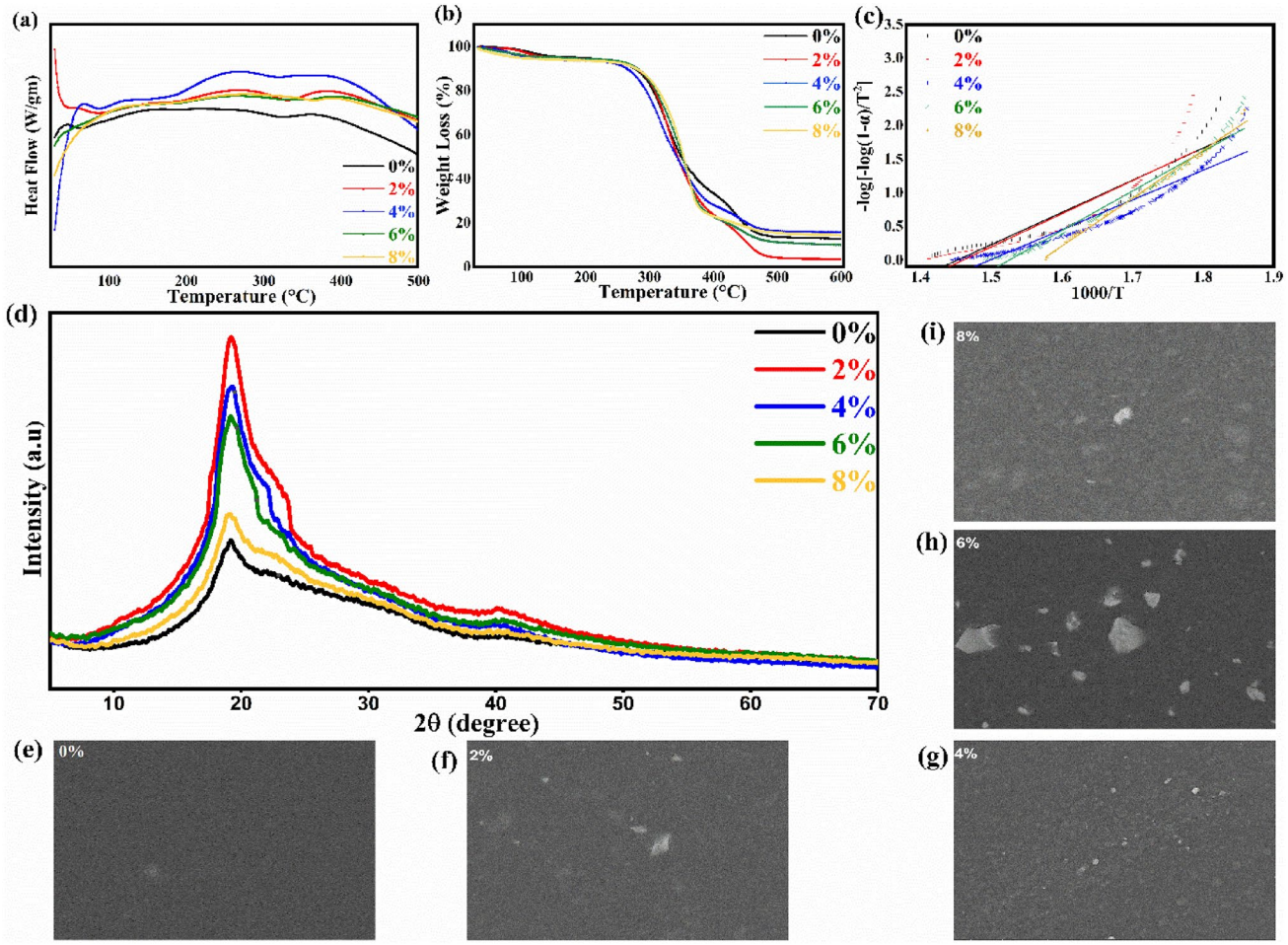

Fig. 3 **a** DSC curve; **b** TGA curve; **c** Coates and Redfern relation; **d** XRD patterns; (e: i) SEM images, of $PVA_{-xwt.\%}SiO_2$

Table 2 The thermal activation energy E_{at} values of $PVA_{-xwt.\%}SiO_2$

Samples (wt.%)	Eat (Kcal mol^{-1})
0	89.538
2	92.08
4	82.83
6	109.9
8	133

be attributed to the increasing of E_{at} with increased SiO_2 concentration except $_{4wt.\%}SiO_2$. Figure 3d shows the XRD pattern of $PVA_{-xwt.\%}SiO_2$ composite; the pristine PVA displays an orthorhombic lattice with a semi-crystalline peak at approximately $2\theta = 20^{\circ}$ match (101) reflection plan [42–45]. The peak became weaker and bordered after adding SiO_2 due to the disruption of intermolecular hydrogen bonding of PVA chains [31]. Figure 3e–i shows the SEM images of $PVA_{-xwt.\%}SiO_2$ composite film; pure PVA displays a smooth and flawless surface, while $PVA_{-xwt.\%}SiO_2$ displays a homogeneous distribution of the nanomaterials in the polymer matrix without creating large aggregations within the polymer matrix which may be attributed to the perfect interaction via hydrogen bonding between the OH groups of PVA molecules and the surface OH groups of SiO_2 nanoparticles[32].

For the next study, create a new electrolyte based on PVST-yEHA. Figure 4a–c shows the FTIR spectra of PVST-$_y$EHA, where only change observed for the band at 636.6 cm^{-1} which was shifts to higher value with an increase in EHA. Figure 4d shows the fitting curves of $(\alpha h\nu)^2$ versus hυ of PVST-$_y$EHA, and the values of E_g are listed in Table 3. Figure 4e shows the K versus λ curve of PVST-$_y$EHA; it has appeared that the extinction coefficient (k) decreases in the range λ = 200–235 nm, then increases in the range λ = 235–1100 nm. Figure 4f shows n versus λ of

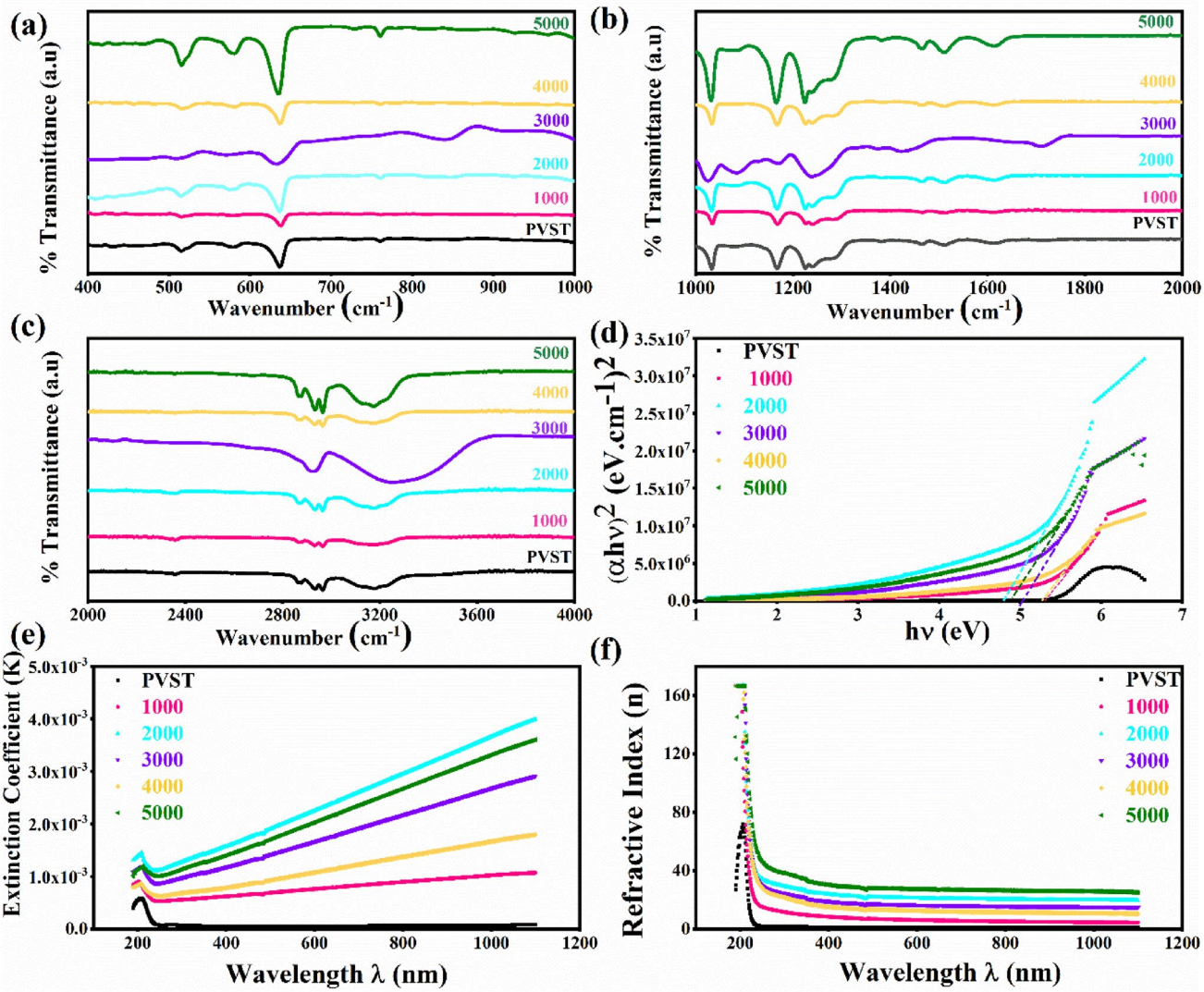

Fig. 4 FTIR spectra **a** 400 to 1000 cm^{-1}; **b** 1000 to 2000 cm^{-1}; **c** 2000 to 4000; **d** refractive index versus wavelength; (e) Extinction coefficient versus wavelength; of PVST-$_y$EHA

Table 3 Values of band gap E_g and activation energy E_a of PVST-yEHA

y (μL)	E_g(eV)	E_a(eV)
0	5.544	0.026
1000	5.36	0.041
2000	4.82	0.078
3000	5.06	0.062
4000	5.29	0.04
5000	4.98	0.072

PVST-$_y$EHA, the curves indicate that n decreases with wavelength increase, while increases with increases $_y$EHA except $y = 3000,4000$ μL decreases with increases n. Figure 5a shows the XRD pattern of PVST-$_y$EHA; the peak at ~$2\theta = 20^{\circ}$ become more bordered after adding MgTIF, which means the crystallinity decreases with added MgTIF. Some peaks appear after adding EHA, which causes some aggregations resulting from the separation of salt from polymer, as shown in the XRD pattern. Figure 5b–g shows the SEM images of PVST-$_y$EHA; PVST is relatively smoother compared to PVST-$_y$EHA, which displays aggregations with irregular tiny pores appearing after increasing the concentrations of $_y$EHA above $y = 3000$ μL. Figure 6a shows the voltage versus time (Stripping/Plating curve) of Mg|SPE_EHF|Mg half cells symmetrical cell at 0.02 mA/cm^2. It can be noticed that the cell with $y = 3000$ μL

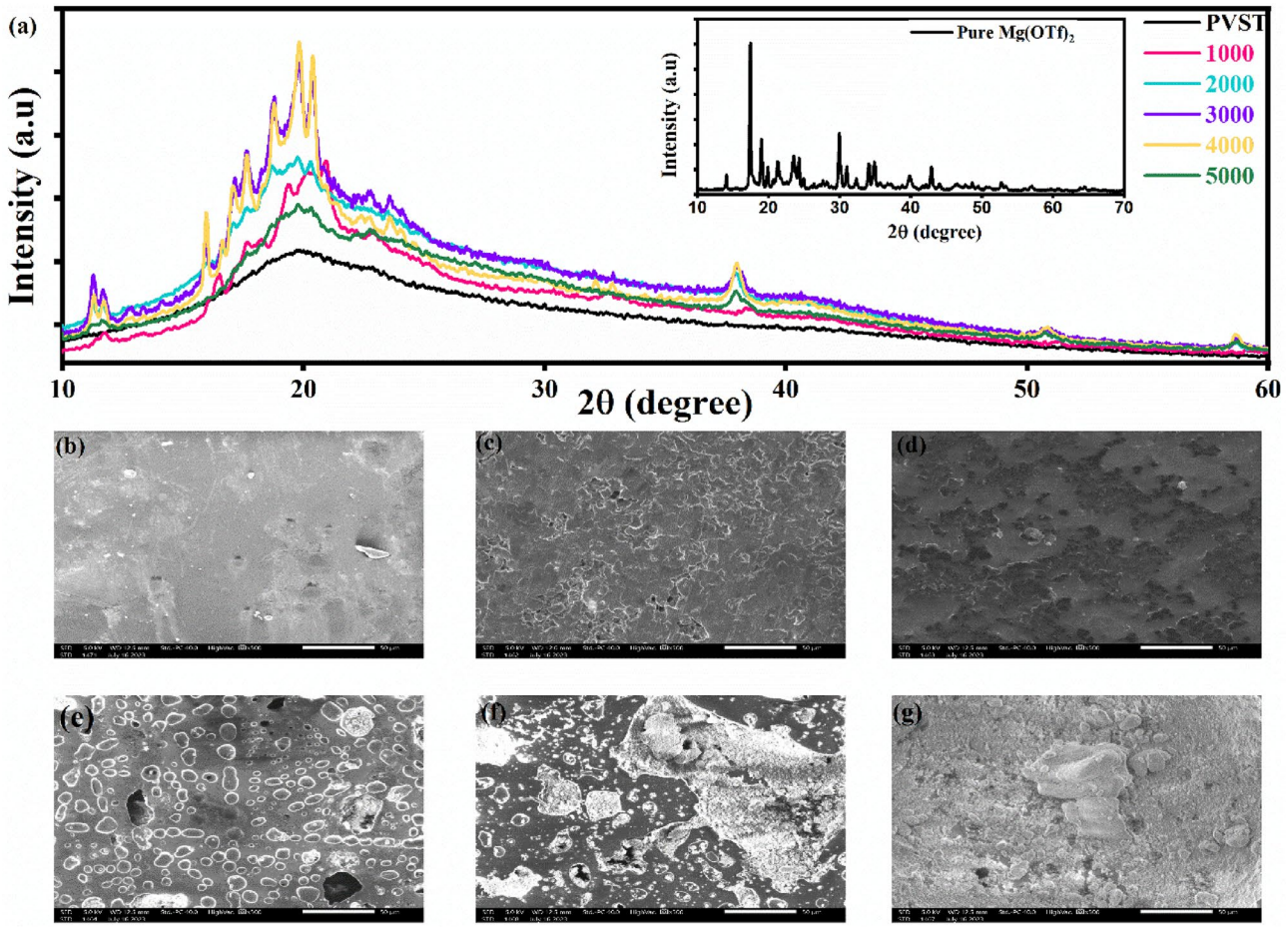

Fig. 5 **a** XRD patterns; SEM of PVST-yEHA **b** y = zero; **c** y = 1000 μL; **d** y = 2000 μL; **e** y = 3000 μL; **f** y = 4000 μL; **g** y = 5000 μL

displays a lower overpotential voltage > 1 V up to over 100 h compared with the other EHA ratios. Figure 6b shows the Nyquist plot of SS|SPE_EHF|SS cells: the equivalent circuit might consist of contact resistance (R_s) and bulk resistance (R_b) in parallel with bulk double-layer capacitance and constant phase element (CPE, the bulk resistance R_b, which is determined from the intersection of the semicircle to the real axis at lower frequencies by used Z-View software. The ionic conductivity was calculated by $\sigma = \frac{t}{R_b * A}$, where R_b is the bulk resistance, t is the thickness of the electrolyte, and A is the surface area of the film.

The study examined how temperatures ranging from room temperature to 65 °C affect the ionic conductivity of PVST-$_y$EHA. The activation energy E_a of Mg^{2+} ions determined from the Arrhenius equation given by $\sigma = \sigma_o \exp^{\frac{-E_a}{KT}}$, where σ, σ_0, T, K, and E_a are the ionic conductivity, pre-exponential factor, absolute temperature, Boltzmann constant, and activation energy, respectively. Figure 6c shows ln σ versus 1000/T; conductivity increases with increasing temperature across all complexes, which may be explained by the free-volume model[46–48], E_a was estimated using the linear least square fitting slope as listed in Table 3. Relaxation time τ was calculated by [35] $\tau = 1/(2\pi f_{max})$, where f_{max} is the relaxation frequency. Figure 6d shows ln τ versus 1000/T curves; the relaxation time decreases with increasing temperature due to the medium's viscosity changes with heat agitation. According to our previous results, PVST-$_{3000}$EHA was chosen as the optimum concentration for the next study. Figure 7a shows the current versus potential curve (LSV curve) of Mg|SPE_EHF|SS cells response in the potential window of 5 V; there is no significant change in current value as the potential hits 3.08 V at room temperature then a sudden spike in current value is noticed, the oxidation of *y* = 3000 μl begins at 3.08 V, as well as the

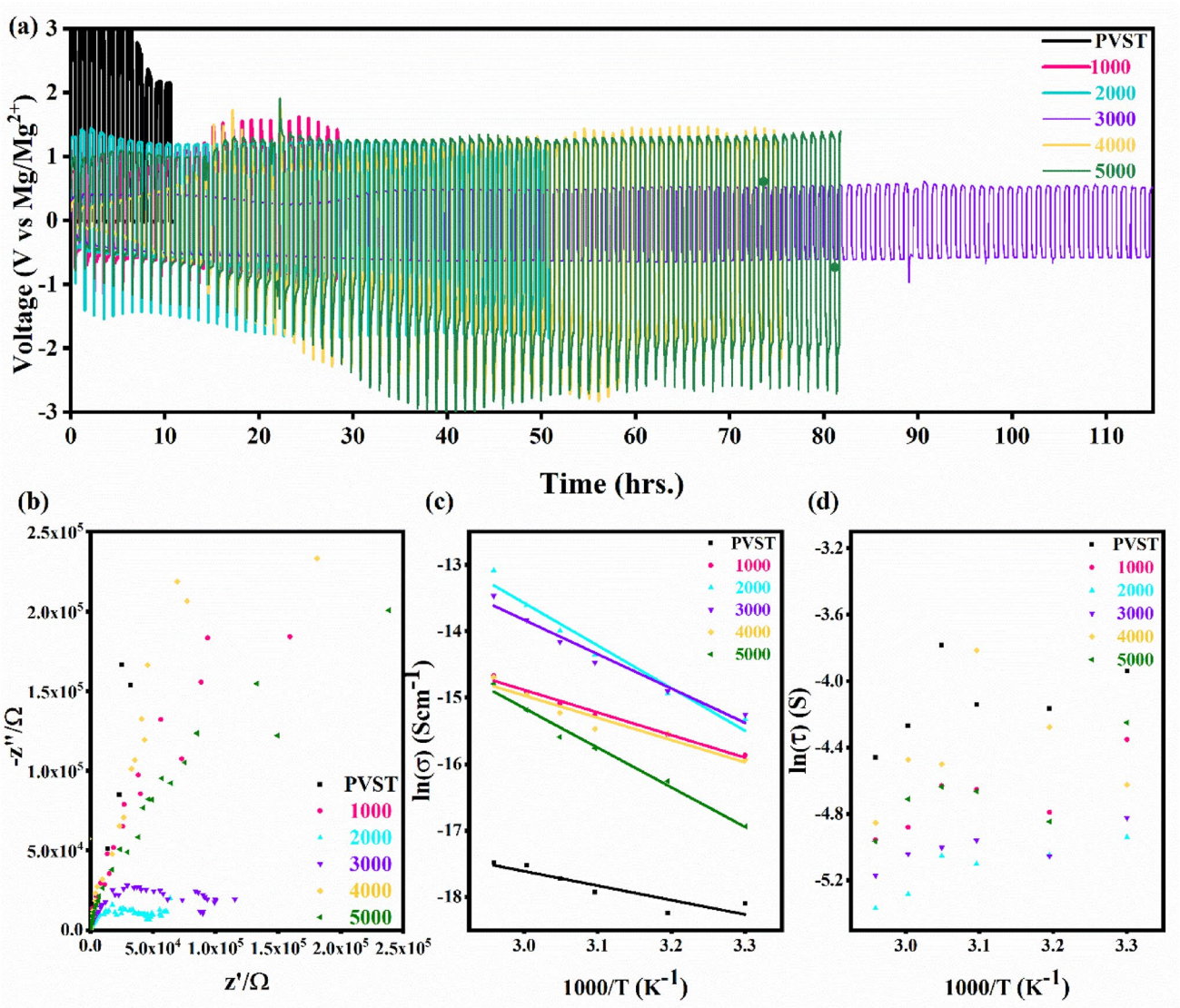

Fig. 6 **a** S.P curves; **b** Nyquist plots; **c** Temperature-dependent of ionic conductivity; **d** ln τ versus 1000/T; of PVST-$_y$EHA

decomposition voltage (V_d). Figure 7b shows the Nyquist plot of Mg|SPE_EHF|Mg half cells before and after the polarization at room temperature. Figure 7c shows a zoomed semicircle in the Nyquist plot of Mg|SPE_EHF|Mg half cells.

The ion transference number $t_{Mg^{2+}}$ calculated by the Bruce-Vincent equation[49]: $t_{Mg^{2+}} = \left[\frac{I_s(\Delta V - R_0 I_0)}{I_0(\Delta V - R_s I_s)}\right]$, where R_0, R_s*and* I_0, I_s refer to the initial current, the initial and steady-state charge-transfer resistances, and the initial current, the steady-state current, respectively. Figure 7d shows the dc polarization curve versus time Mg|SPE_EHF|Mg half cells at room temperature, the current decline over time until it achieves a steady-state, and the ion transference number $t_{Mg^{2+}}$ = 0.88 for y = 3000µl. Figure 8 sketches the Mg|PVST$_{_3000}$EHA_HFE|S full cell design, and it will be denoted by Mg|SPE_EHF|S; Fig. 9a shows the CV curve of Mg|SPE_EHF|S cell at a scan rate of 0.02 Vs^{-1} and a potential window from 0 to 2.6 V for the first six cycles. The cathodic current is very large compared to the anodic current. Figure 9b shows the CV curves for the first and second cycles; the anodic peak current densities ~ 0.247 $mA.cm^{-2}$ and 0.174 $mA.cm^{-2}$ are observed at 2.1 V and 2.13 V, and the cathodic peak current densities ~ 0.29 $mA.cm^{-2}$ and 0.212 $mA.cm^{-2}$ are observed at 0.422 V, 0.494 V for the first and second cycle,

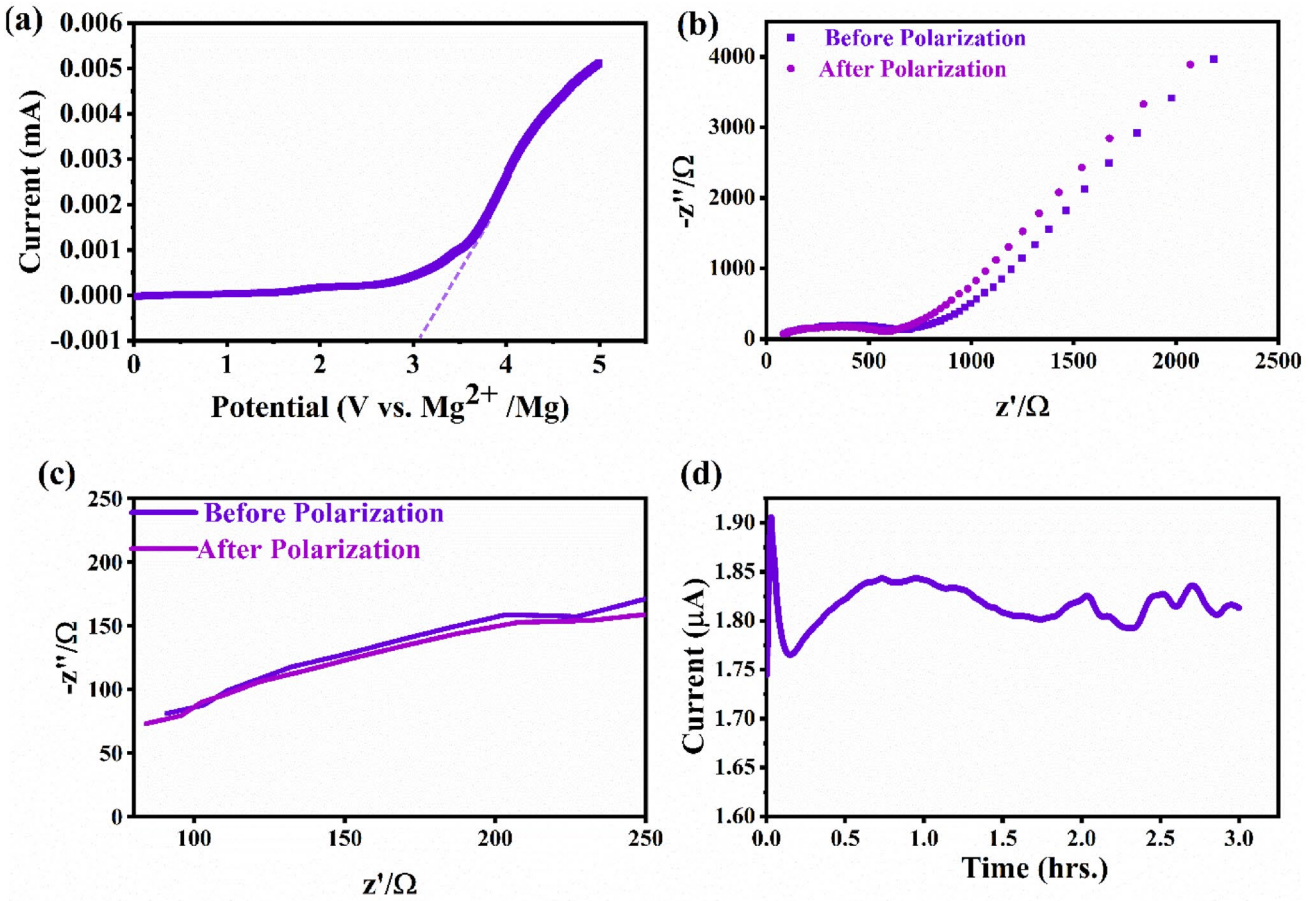

Fig. 7 **a** LSV curve; **b** Nyquist plots before and after polarization; **c** zoomed semicircle in Nyquist plots; **d** DC polarization curve versus time, all curves of $PVST_{-3000}EHA$

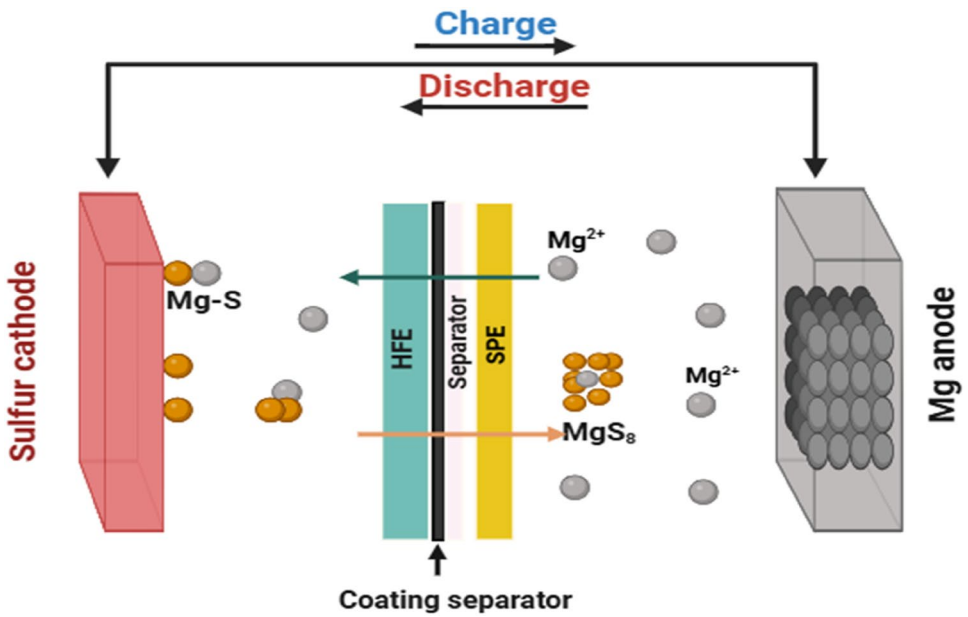

Fig. 8 Full cell Mg|SPE_EHF|S cell of Mg-S battery

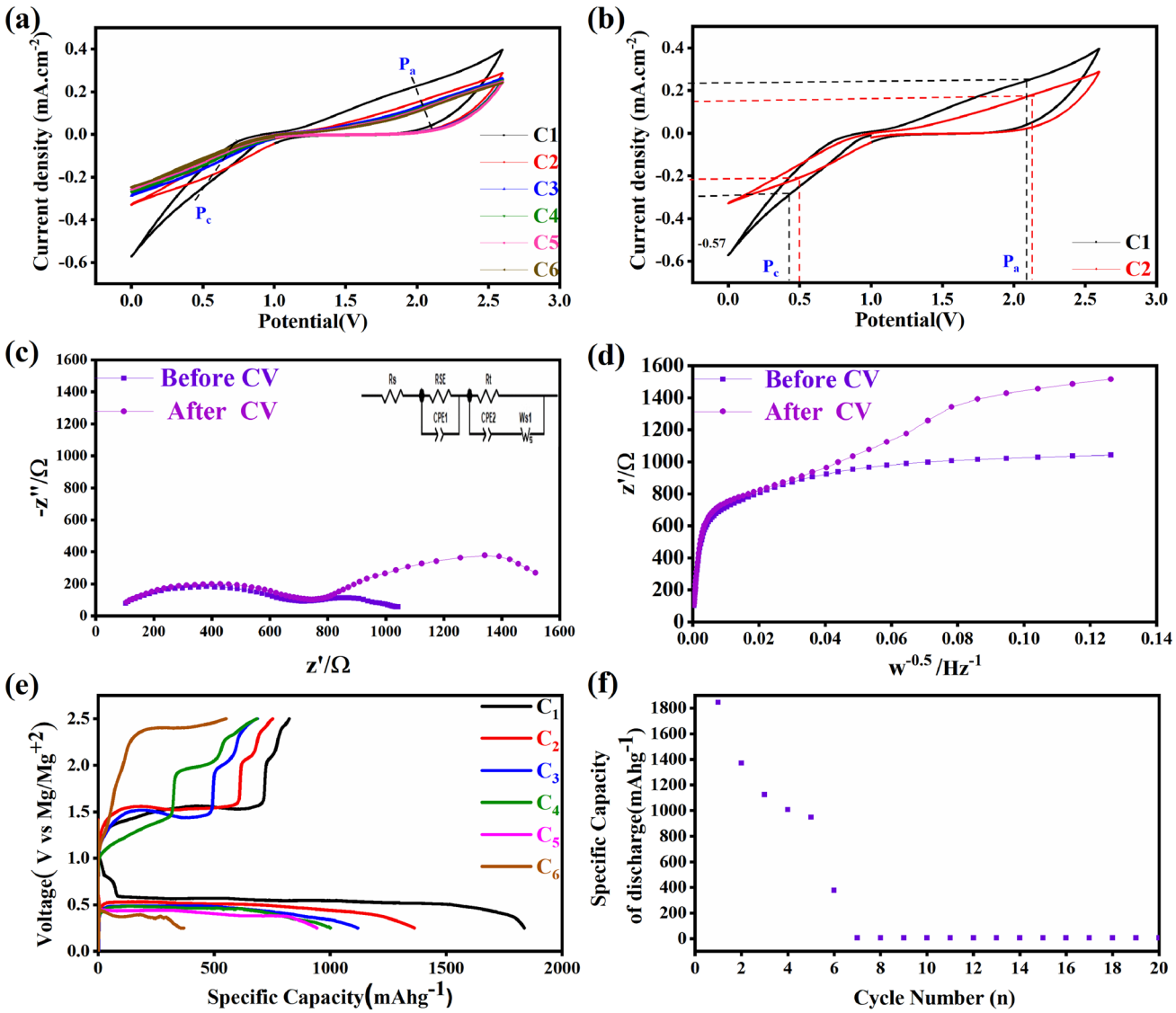

Fig. 9 **a** CV curve; **b** CV for the first and second cycle; **c**-Z″ versus Z′ and its equivalent circuit (inset); **d** linear fitting of Warburg impedance; **e** Galvanostatic discharge–charge curve; **f** Specific capacity of discharge versus cycle number, of PVST-$_{3000}$EHA

respectively. Figure 9c shows the Nyquist plot of Mg|SPE_EHF|S cell before and after CV at room temperature; the fitting equivalent circuit stimulated by Z-View software is inset, where R_s, R_{SEI}, R_{ct}, CPE_1, CPE_2, A_w and $D_{Mg^{2+}}$ are referred to as the bulk resistance (representing high-frequency intercept), the interphase resistance, the charge-transfer resistance, Warburg impedance (representing low-frequency intercept), and the diffusion coefficient, respectively; the impedance parameters are listed in Table 4. Figure 9d shows the linear fitting $\omega^{-0.5}$ versus Z` (real part impedance) at low frequencies of the relation $Z\} = R_s + R_{ct} + A_w w^{-0.5}$, where the Warburg factor A_w is obtained from the slope of the lines, then

Table 4 Electrochemical impedance parameters of PVST$_{-3000}$EHA

EIS parameters	$R_s(\Omega)$	$R_{SEI}(\Omega)$	$R_{ct}(\Omega)$	CPE_1 (F)	CPE_2 (F)	A_w (Ω)	$D^{2+}_{Mg}[cm^2.s^{-1}]$
Before	40.084	663.27	743.46	3.1386×10^{-7}	0.00039475	674.079	3.19×10^{-15}
After	38.17	733.8	755.2	4.016×10^{-7}	0.00023912	3060.53	7.8×10^{-16}

substituting in the diffusion coefficient equation [50] $D_{Mg^{2+}} = \left[\frac{R^2T^2}{2A^2n^4F^4C^2A_w^2}\right]$, where R = 8.314 J/mol K, T = 328 K, A = 1.5 cm^2, and n, F = 96,485 C mol^{-1}, and C are gas constants, absolute temperature, the cathode area in touch with the electrolyte, the number of electrons involved, the Faraday constant, and the concentration of magnesium ions (mol/cm^3), respectively. The values of $D_{Mg^{2+}}$ are 3.19×10^{-15} and 7.8×10^{-16} before and after CV, respectively, where the $D_{Mg^{2+}}$ decrease after CV due to the creation of a high interface kinetics barrier. Figure 9e shows the galvanostatic discharge–charge curve of Mg|SPE_EHF|S cell at a current density of 0.02 $mA.cm^{-2}$.

The initial capacity of 1837 $mAhg^{-1}$ for the first cycle and 376 $mAhg^{-1}$ for the sixth one, the electrolyte retains 20.4% of its initial capacity after six cycles. The discharge capacity reduction during cycling might be related to the high sulfur loading at the cathode and the sluggish kinetics of cathode redox processes, which hinder the entire exploitation of the active material[51]. Figure 9f shows the full cell's specific capacity versus cycle number, where the capacity decreases with increased cycle number and fades after the six cycles. Table 5 compares the ionic conductivity, specific capacity, electrochemical stability, and transference number of our work to other literature in this area, the comparison confirms the value of the current innovative aspect. To follow the structure and morphology evolution of the S-cathode at various electrochemical states extracted from full cell Mg|SPE_EHF|S was discharged to 0.1 V, and from other full cell Mg|SPE_EHF|S was discharged/ charged (magnesiation/ de-magnesiation) to 0.1/2.5 V, then cathode cleaned by ACN and dried at 80° for 1 h. The pristine, discharged, and discharged/charged cathodes are denoted as S_0, S_1, and S_2, respectively. Figure 10a shows XRD patterns of pure S powder, pure SiC powder, pure GNPs powder, S_0, S_1, and S_2; it can be noticed that the main peaks of sulfur powder at 2θ ~ 23° and 28° were assigned to (222) and (040) reflection plans, respectively. All the diffraction peaks match well the F_{ddd} orthorhombic phase of pure sulfur (JCPDS no. 08–0247) [52–54]. The characteristic diffraction peaks of S decreased after treatment with the microwave in S_0 because the vaporization of S on the surface of GNP and SiC disrupts its periodic structure.

The XRD pattern of SiC shows the main peaks at 2θ ~ 35.7° and 60° assigned to (111) and (220) reflection plans (JCPDS no. 29–1129)[55], and the main peaks of GNPs 2θ ~ 26.4° assigned to (002) reflection plans (JCPDS no.02–0212)[56, 57]. To follow the structure evolution of S_0 with Mg^{2+} insertion/extraction, Fig. 10b shows zoomed-in at 2θ ~ 35.7° of SiC peak; the peak intensity increases after magnesiation (S_1) and decreases after de-magnesiation. The decrease in the SiC peak's intensity after the magnesiation process can be attributed to the formation of bonds between Mg and S forming MgS_n at the expense of the SiC—S bonds. After the de-magnesiation process, some Mg atoms detach from S and return to the anode while S atoms return to stack on the surface of SiC, which reduces the peak intensity of SiC. X-ray profile analysis is an effective approach for estimating crystallite size and lattice strain using the Williamson-Hall (W–H) equation [58, 59]:

$\beta_{hkl}\cos(\theta) = 4\varepsilon\sin(\theta) + \frac{k\lambda}{D}$, where D = crystalline size, K = shape factor (0.9), λ = wavelength of XRD, β = the full width at high maximum, and ε = the strain. Figure 10c shows 4sin(θ) versus $\beta_{hkl}\cos(\theta)$

Table 5 summary of ionic conductivity, specific capacity, electrochemical stability, and transference number of solid-state electrolytes

Mg salt	Polymer host	Ionic conductivity (S cm^{-1} at RT)	Specific capacity (mAh g^{-1})	Electrochemical stability	Transference number	References
MgTIF	PVA	~ 10^{-7}	1837	3.08 V	0.88	Our work
MgTIF	polyvinylidene fluoride (PVDF)	~ 10^{-5}	530	–	0.8 at 55 °C	[60]
MgTIF	poly(ethylene oxide) (PEO)	1.6×10^{-5}	–	–	0.37	[61]
MgTIF	Polymethyl methacrylate (PMMA)	1.50×10^{-4}	–	3.2 V	–	[62]
MgTIF	PVDF	5.11	–	3.5	0.27	[63]
MgTIF	PVDF	4.0	–	4.1		[64]
MgTIF	PVDF	4	–	3.3	0.66	[65]
MgTIF	PVA	5.41×10^{-4}	–	–	–	[24]

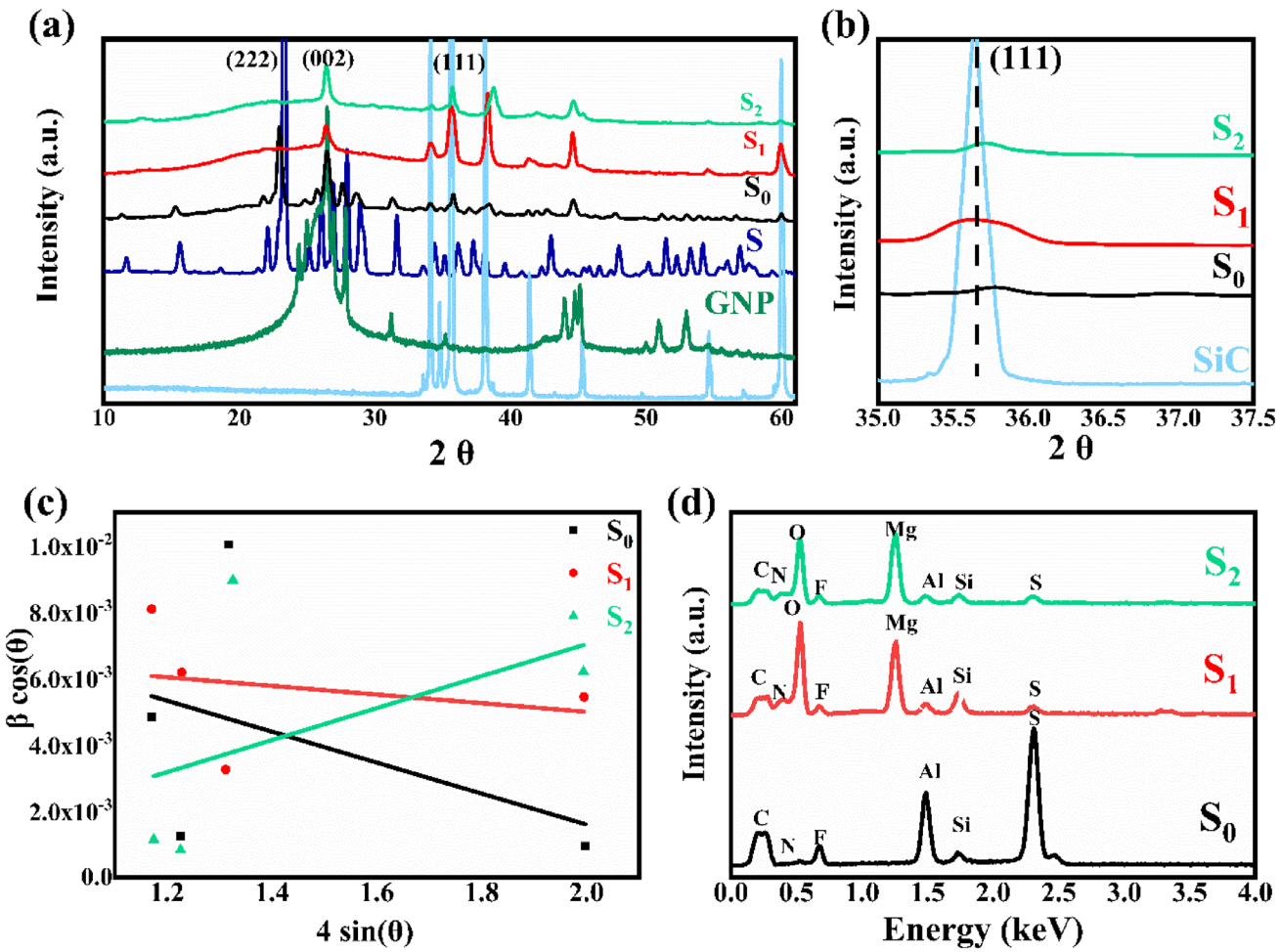

Fig. 10 **a** XRD patterns of pure S powder, pure SiC powder, pure GNPs powder, S_0, S_1, and S_2; **b** XRD zoomed of SiC peak at 2θ ~35°—37.5°; **c** W–H plot; **d** EDX of S_0, S_1, S_2

Table 6 Strain and crystalline size for S_0, S_1, and S_2 by (W–H) plot

Element	S_0	S_1	S_2
Strain (ε) × 10^{-3}	4.67	1.3	4.82
Crystallite size D (nm)	13.29	19.07	55.27

Table 7 The ratio of elements in S_0, S_1, and S_2 extracted from EDS spectra

Element	S_0	S_1	S_3
	Mass%	Mass%	Mass%
C	45.4	4.83	3.5
N	1.59	10	8.77
O	1.82	49.3	46.18
F	8.95	8.27	9.45
Al	10.64	2.73	3.03
Si	1.36	5.19	2.68
S	30.23	2.26	2.93
Mg	Zero	17.42	22.22

fitting lines, where the crystallite size (intercept) and strain values (slope) are listed in Table 6. The value of the macro-strain decreases after magnesiation (S_1) and increases after de-magnesiation (S_2), confirming the conversion reaction's reversibility. Figure 10d shows the EDS spectra of S_0, S_1, and S_2; all elements existed and observed the Al element ratio, also compared between all element ratios in S_0, S_1, and S_2 as listed in Table 7. The results display an increase in the ratio of Mg^{2+} from Zero in S_0 to 17.42 wt.% after discharge in S_1, further increasing to 22.22 wt.% after recharge, and a decrease in the

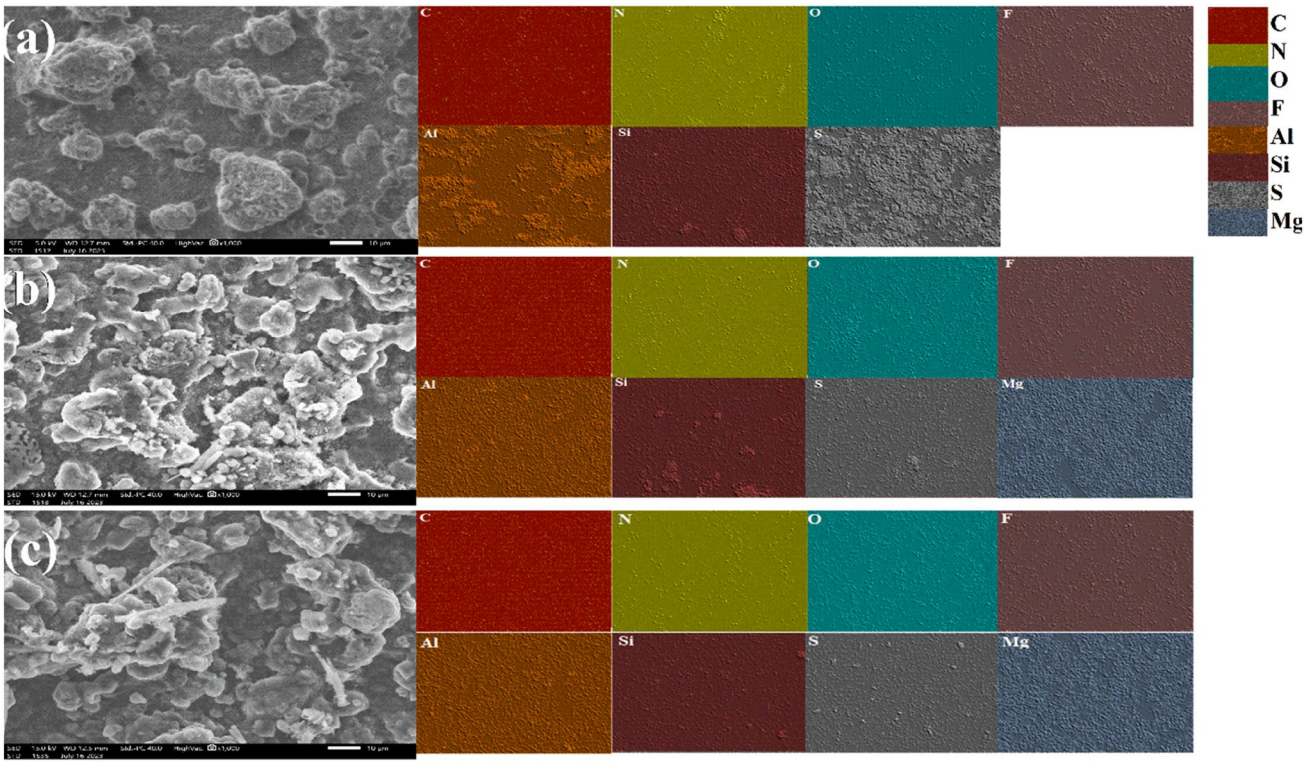

Fig. 11 SEM mapping of S-cathode extracted from Mg|SPE_EHF|S cell. **a** S_0; **b** S_1; **c** S_2

ratio of S from 30.23 wt.% in S_0 to 2.26 wt.% in S_1 and increase to 2.93 wt.% in S_2, the results suggest the largely reversible conversion reaction of the S_8 to polysulfide molecules and vice versa. Figure 11a–c shows SEM images and mapping for S_0, S_1, and S_2; S_0 displays an inhomogeneous aggregation due to the vaporization of S on the surface of GNP and SiC, S_1 displays a medium – cauliflower with some sedimentations due to the conversion reaction of S_8 polysulfides MgS_n, while S_2 cauliflower morphology with low sedimentations, this because the cathode retained some Mg^{2+} during the de-magnesiation process. The mapping chart displayed a decrease in the distribution of sulfur elements on the surface after the magnesiation process and an increase after de-magnesiation. From all the previous results for the cathode, we concluded the Mg^{2+} was not extracted from the S-cathode during the de-magnesiation process due to irreversible entrapment.

Mg-anode at various electrochemical states extracted from full cell Mg|SPE_EHF|S was discharged to 0.1 V, and from other full cell Mg|SPE_EHF|S was discharged/ charged (magnesiation/ de-magnesiation) to 0.1/2.5 V, then anode cleaned by ACN and dried at 80° for 1 h. The pure Mg, interface after magnesiation, and interface e after de-magnesiation are shorted as Mg_0, Mg_1, and Mg_2, respectively.

Figure 12a shows the XRD pattern for Mg_0 and Mg_1, Mg_2; it can be noticed that the main peaks of Mg at 2θ ~ 32.2°, 34.3°, 36.6°, 47.8°and 63° assigned to (100), (002), (101), (102) and (103) reflection plans of the hexagonal Mg (JCPDS no. 90–3058)[66], the intensity of the peaks increased after magnesiation and reduced after de-magnesiation. Figure 12b shows zoomed-in at 2θ ~ 34.3° of the main peak of Mg; the peak shifted to the left after magnesiation and further moved to the left after de-magnesiation. Figure 12c shows EDS spectra of Mg_0, Mg_1, and Mg_2; the results display an increase of S to 0.33 wt.% after magnesiation and further increased to 0.87 wt.% after de-magnesiation as listed in Table 8. The results confirm the partial dissolution of sulfur within the electrolyte upon assembling the cell and the shuttle effect of magnesium polysulfide after recharge [67]. Figure 12d–f shows SEM mapping of Mg_0, Mg_1, and Mg_2; Mg_0 displays a homogeneous and smooth surface, Mg_1 displays low-density aggregation, and Mg_2 displays high-density aggregation.

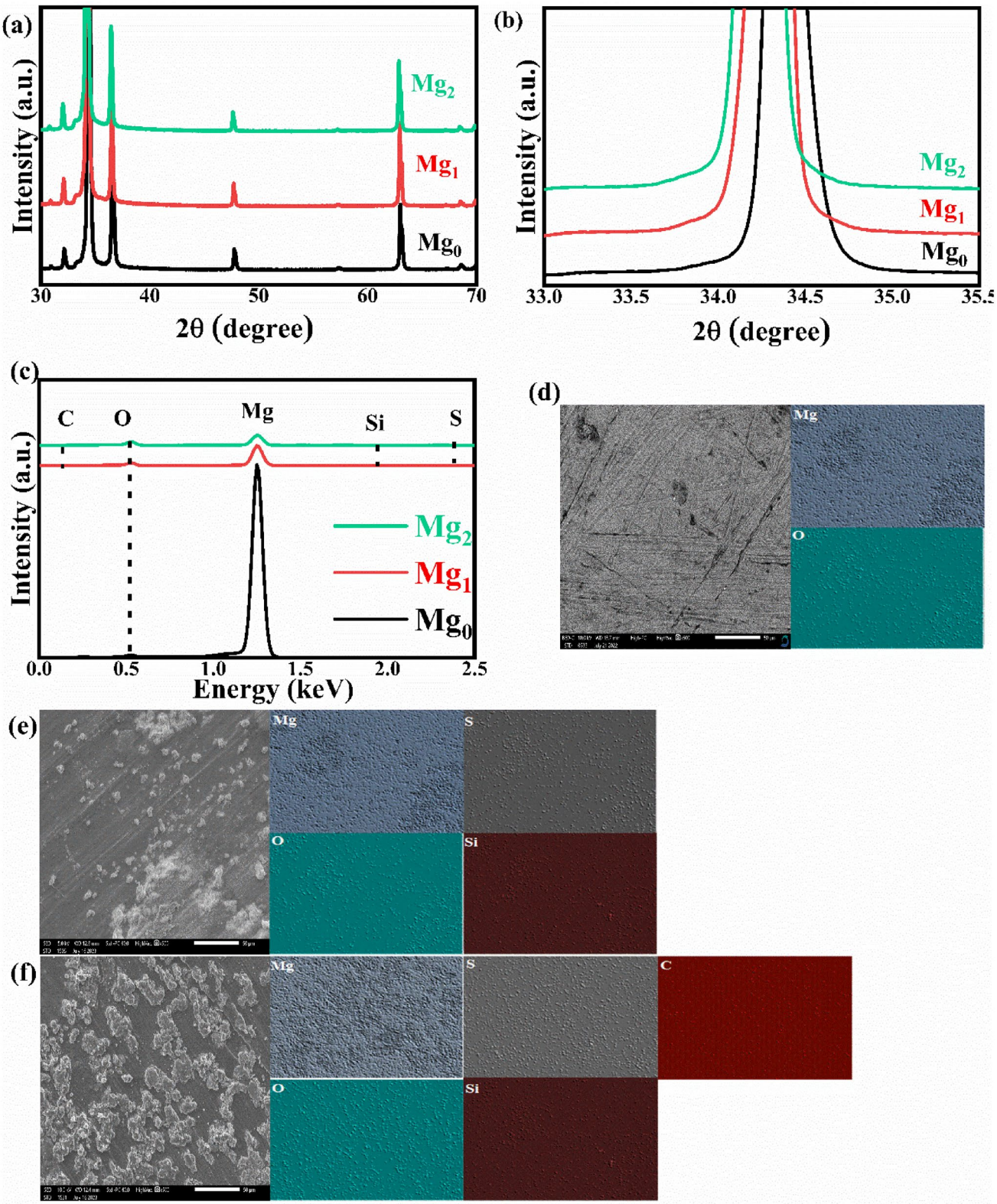

Fig. 12 **a** XRD patterns for anode; **b** XRD zoomed of Mg main peak at 2θ ~ 34.3°; **c** EDS spectra; SEM mapping of **d** Mg_0; **e** Mg_1; **f** Mg_2, extracted from Mg|SPE_EHF|S cell

Table 8 The ratio of elements in Mg_0, Mg_1, and Mg_2 extracted from EDS spectra

Element	Mg_0	Mg_1	Mg_2
	Mass%	Mass%	Mass%
O	0.83	25.7	42.37
Mg	99.17	73.9	49.95
C	–	–	6.22
S	–	0.33	0.87
Si	–	0.07	0.59

4 Conclusion

In this paper, the magnesium-sulfur (Mg-S) battery is based on probing the role of EHA in modifying the physiochemical properties of SPEs based on PVA, SiO_2, and MgTIF. The introduction of EHA improves the conductivity and reduces the S.P overpotential. PVST-$_{3000}$EHA displayed the optimum electrochemical performance, such as a high ionic transference number $\left(t_{mg^{2+}} = 0.88\right)$, and minimal overpotential over 100 h. The Mg-S battery based PVST_3000EHA exhibits a high initial discharge-specific capacity in the first cycle up to 1837 $mAhg^{-1}$, and over six cycles, it maintained a reversible capacity of 376 $mAhg^{-1}$. Furthermore, solid-state electrolytes can significantly enhance the safety of Mg-S batteries, making them suitable for large-scale applications and meeting future energy storage requirements. Mg-anode at various electrochemical states was extracted from full cell Mg|SPE_EHF|S, shows an increase of S after magnesiation and further increased after de-magnesiation. The results confirm the partial dissolution of sulfur within the electrolyte upon assembling the cell and the shuttle effect of magnesium polysulfide after recharge. Much work must be done to overcome the limits of the current work such as the low ionic conductivity, high stripping/plating overpotential, and the high interfacial diffusion barrier.

Acknowledgements

This work was supported by Bibliotheca Alexandrina/ASRT (Grant No. 1530)

Author contributions

S.Y. Ibrahim: Writing – original draft, Methodology. S Abouelhassan: Writing – review & editing. E. Sheha: Supervision, Conceptualization, Investigation, Writing – original draft, Writing – review & editing.

Funding

Open access funding provided by The Science, Technology & Innovation Funding Authority (STDF) in cooperation with The Egyptian Knowledge Bank (EKB). Bibliotheca Alexandrina/ASRT,1530,Eslam MOHAMED MAHMOUD Sheha

Data availability

All data generated or analyzed during this study are included in this published article.

Declarations

Conflict of interests The authors declare that they have no financial interests to disclose that could influence the publication of this work.

Ethical approval All ethical standards are strictly adhered to in this work.

References

1. L. Kong, C. Yan, J.Q. Huang, M.Q. Zhao, M.M. Titirici, R. Xiang et al., A review of advanced energy materials

for magnesium–sulfur batteries. Energy Env. Mater. **1**, 100–112 (2018)
2. C.-X. Zu, H. Li, Thermodynamic analysis on energy densities of batteries. Energy Environ. Sci. **4**, 2614–2624 (2011)
3. V.B. Parambath, Z. Zhao-Karger, T. Diemant, M. Jäckle, Z. Li, T. Scherer et al., Investigation on the formation of Mg metal anode/electrolyte interfaces in Mg/S batteries with electrolyte additives. J. Mater. Chem. A **8**, 22998–23010 (2020)
4. Y. Yao, Y. Li, Y. Zhan, Z. Li, Z. Li, R.M. Laine et al., Probing the effect of Se doping in S cathode for high performance Mg-S batteries. Chem. Eng. J. **499**, 156682 (2024)
5. J.T. Lee, Y. Zhao, S. Thieme, H. Kim, M. Oschatz, L. Borchardt et al., Sulfur-infiltrated micro-and mesoporous silicon carbide-derived carbon cathode for high-performance lithium sulfur batteries. Adv. Mater. **25**, 4573–4579 (2013)
6. L. Sheng, J. Feng, M. Gong, L. Zhang, J. Harding, Z. Hao et al., Advances and challenges in electrolyte development for magnesium-sulfur batteries: a comprehensive review. Molecules **29**, 1234 (2024)
7. J. Wang, Z. Zhao, R. Muchakayala, S. Song, High-performance Mg-ion conducting poly (vinyl alcohol) membranes: preparation, characterization and application in supercapacitors. J. Membr. Sci. **555**, 280–289 (2018)
8. Y. Guo, S. Wu, Y.-B. He, F. Kang, L. Chen, H. Li et al., Solid-state lithium batteries: safety and prospects. EScience **2**, 138–163 (2022)
9. H. Du, S. Li, H. Qu, B. Lu, X. Wang, J. Chai et al., Stable cycling of lithium-sulfur battery enabled by a reliable gel polymer electrolyte rich in ester groups. J. Membr. Sci. **550**, 399–406 (2018)
10. Y. Cui, W. Chen, W. Xin, H. Ling, Y. Hu, Z. Zhang et al., Gradient quasi-solid electrolyte enables selective and fast ion transport for robust aqueous zinc-ion batteries. Adv. Mater. **36**, 2308639 (2024)
11. Z. Chen, W. Zhao, Q. Liu, Y. Xu, Q. Wang, J. Lin et al., Janus quasi-solid electrolyte membranes with asymmetric porous structure for high-performance lithium-metal batteries. Nano-Micro Letters **16**, 114 (2024)
12. S. Chen, Z. Zhang, L. Li, W. Yuan, Covalently-bonded poly (vinyl alcohol)-silica composite nanofiber separator with enhanced wettability and thermal stability for lithium-ion battery. ChemistrySelect **3**, 13365–13371 (2018)
13. S.B. Aziz, O.G. Abdullah, S.A. Hussein, H.M. Ahmed, Effect of PVA blending on structural and ion transport properties of CS: AgNt-based polymer electrolyte membrane. Polymers **9**, 622 (2017)
14. M. Brza, S.B. Aziz, S. Raza Saeed, M.H. Hamsan, S.R. Majid, R.T. Abdulwahid et al., Energy storage behavior of lithium-ion conducting poly (vinyl alcohol)(PVA): Chitosan (CS)-based polymer blend electrolyte membranes: preparation, equivalent circuit modeling, ion transport parameters, and dielectric properties. Membranes **10**(381), 2020 (2020)
15. H.A. Hoang, D. Kim, High performance solid-state lithium-sulfur battery enabled by multi-functional cathode and flexible hybrid solid electrolyte. Small **18**, 2202963 (2022)
16. X.-W. Wu, M. Seenivasan, C. Karuppiah, B.-R. Zhang, J.-Y. Shih, Y.-J. J. Li, *et al.*, "Fabrication electro-spun poly (vinyl alcohol)-Melamine Nonwoven Membrane composite separator for high-power lithium-ion batteries," *Heliyon,* 2024.
17. Y.-J. Yang, R. Wang, J.-X. Xue, F.-Q. Liu, J. Yan, S.-X. Jia et al., In situ forming asymmetric bi-functional gel polymer electrolyte in lithium–sulfur batteries. J. Mater. Chem. A **9**, 27390–27397 (2021)
18. B.A. Abdulkadir, J. Ojur Dennis, Y. Al-Hadeethi, M.F.B.A. Shukur, E.M. Mkawi, N. Al-Harbi et al., Optimization of the electrochemical performance of a composite polymer electrolyte based on PVA-K2CO3-SiO2 composite. Polymers **13**, 92 (2020)
19. B. McLean and I. Yarovsky, "Structure, Properties, and Applications of Silica Nanoparticles: Recent Theoretical Modeling Advances, Challenges, and Future Directions," *Small,* p. 2405299, 2024.
20. J. Chen, S. Tan, L. Li, G. Huang, J. Wang, F. Pan, The metamorphosis of Mg (SO3CF3) 2-based electrolytes for rechargeable magnesium batteries. ChemElectroChem (2024). https://doi.org/10.1002/celc.202300664
21. D.-T. Nguyen, A.Y.S. Eng, M.-F. Ng, V. Kumar, Z. Sofer, A.D. Handoko et al., A high-performance magnesium triflate-based electrolyte for rechargeable magnesium batteries. Cell Rep. Phys. Sci. **1**, 100265 (2020)
22. S.-B. Son, T. Gao, S.P. Harvey, K.X. Steirer, A. Stokes, A. Norman et al., An artificial interphase enables reversible magnesium chemistry in carbonate electrolytes. Nat. Chem. **10**, 532–539 (2018)
23. D. Zhang, S. Duan, X. Liu, Y. Yang, Y. Zhang, W. Ren et al., Deeping insight of Mg (CF3SO3) 2 and comprehensive modified electrolyte with ionic liquid enabling high-performance magnesium batteries. Nano Energy **109**, 108257 (2023)
24. S.-K. Jeong, Y.-K. Jo, N.-J. Jo, Decoupled ion conduction mechanism of poly (vinyl alcohol) based Mg-conducting solid polymer electrolyte. Electrochim. Acta **52**, 1549–1555 (2006)
25. X. Xue, R. Chen, C. Yan, P. Zhao, Y. Hu, W. Kong et al., One-step synthesis of 2-ethylhexylamine pillared vanadium disulfide nanoflowers with ultralarge interlayer spacing for

high-performance magnesium storage. Adv. Energy Mater. **9**, 1900145 (2019)
26. S.S. Birajdar, S. Naqvi, K.S. More, A.L. Puyad, R. Kumar, S.V. Bhosale et al., Influences of the number of 2-ethylhexylamine chain substituents on electron transport characteristics of core-substituted naphthalene diimide analogues. New J. Chem. **45**, 1590–1600 (2021)
27. F. Li, J. Zhao, Three dimensional porous SiC for lithium polysulfide trapping. Phys. Chem. Chem. Phys. **20**, 4005–4011 (2018)
28. A. Rosenman, E. Markevich, G. Salitra, D. Aurbach, A. Garsuch, F.F. Chesneau, Review on Li-sulfur battery systems: an integral perspective. Adv. Energy Mater. **5**, 1500212 (2015)
29. Q. Sun, S. Luo, R. Huang, Q. Liu, S. Yan, and X. Lin, "Insights on solid electrolytes for solid-state magnesium batteries: progress and prospects," *Energy Storage Materials,* p. 103508, 2024.
30. J. Li, J. Suo, R. Deng, Structure, mechanical, and swelling behaviors of poly (vinyl alcohol)/SiO2 hybrid membranes. J. Reinf. Plast. Compos. **29**, 618–629 (2010)
31. M. Hatami, M. Ahmadipour, S. Asghari, Heterocyclic grafting functionalization of silica nanoparticles: fabrication, morphological investigation and application for PVA nanocomposites. J. Inorg. Organomet. Polym Mater. **27**, 1072–1083 (2017)
32. T.S. Soliman, S.A. Vshivkov, S.I. Elkalashy, Structural, thermal, and linear optical properties of SiO2 nanoparticles dispersed in polyvinyl alcohol nanocomposite films. Polym. Compos. **41**, 3340–3350 (2020)
33. S.B. Aziz, H.M. Ahmed, A.M. Hussein, A.B. Fathulla, R.M. Wsw, R.T. Hussein, Tuning the absorption of ultraviolet spectra and optical parameters of aluminum doped PVA based solid polymer composites. J. Mater. Sci. **26**, 8022–8028 (2015)
34. A. Hashim, Z. Hamad, Lower cost and higher UV-absorption of polyvinyl alcohol/silica nanocomposites for potential applications. Egypt. J. Chem. **63**, 461–470 (2020)
35. A. Alsaad, A. Ahmad, A.R. Al Dairy, A.S. Al-anbar, Q.M. Al-Bataineh, Spectroscopic characterization of optical and thermal properties of (PMMA-PVA) hybrid thin films doped with SiO2 nanoparticles. Results Phys. **19**, 103463 (2020)
36. F.-Y. Quan, L.-L. Chen, Y.-Z. Xia, Q. Ji, Structure and properties of PVA/SiO2 interpenetrating polymer network materials prepared by the sol-gel method. Polym. Polym. Compos. **17**, 97–100 (2009)
37. C.-C. Yang, Y.J. Li, T.-H. Liou, Preparation of novel poly (vinyl alcohol)/SiO2 nanocomposite membranes by a sol–gel process and their application on alkaline DMFCs. Desalination **276**, 366–372 (2011)
38. C.-C. Yang, Synthesis and characterization of the cross-linked PVA/TiO2 composite polymer membrane for alkaline DMFC. J. Membr. Sci. **288**, 51–60 (2007)
39. X. Tan, C. Liang, S. Bai, P. Lan, Y. Ren, J. Zhao et al., PVA/silica hybrid hydrogel with ultra-high strength and toughness. J. Mater. Sci. **59**, 6916–6928 (2024)
40. S. Badr, E. Sheha, Impact of hydroquinone on thermal and electrical properties of plasticized [poly (vinyl alcohol)] 0.7 (LiBr) 0.3 (H2SO4) solid acid membrane. Polym. Int. **60**, 1142–1148 (2011)
41. V. Mirzajani, H. Nazarpour-Fard, K. Farhadi, Impacts of titanium dioxide nanoparticles on thermal decomposition kinetics of nitrocellulose-based propellant as a bio-derived polymer. Iran. Polym. J. **33**, 699–710 (2024)
42. Z. Peng, L.X. Kong, S.-D. Li, P. Spiridonov, Poly (vinyl alcohol)/silica nanocomposites: morphology and thermal degradation kinetics. J. Nanosci. Nanotechnol. **6**, 3934–3938 (2006)
43. H. Pingan, J. Mengjun, Z. Yanyan, H. Ling, A silica/PVA adhesive hybrid material with high transparency, thermostability and mechanical strength. RSC Adv. **7**, 2450–2459 (2017)
44. S. Radoor, J. Karayil, J. Parameswaranpillai, S. Siengchin, Adsorption of methylene blue dye from aqueous solution by a novel PVA/CMC/halloysite nanoclay bio composite: characterization, kinetics, isotherm and antibacterial properties. J. Environ. Health Sci. Eng. **18**, 1311–1327 (2020)
45. M. Morad, M. Abo Ghazala, M. El-Shaarawy, M. Gouda, T. Elrasasi, Preparation and characterization of conjugated PVA/PANi blend films doped with functionalized graphene for thermoelectric applications. Sci. Rep. **14**, 16722 (2024)
46. T. Miyamoto, K. Shibayama, Free-volume model for ionic conductivity in polymers. J. Appl. Phys. **44**, 5372–5376 (1973)
47. R. Manjuladevi, S. Selvasekarapandian, M. Thamilselvan, R. Mangalam, S. Monisha, P.C. Selvin, A study on blend polymer electrolyte based on poly (vinyl alcohol)-poly (acrylonitrile) with magnesium nitrate for magnesium battery. Ionics **24**, 3493–3506 (2018)
48. Z. Li, J. Fu, X. Zhou, S. Gui, L. Wei, H. Yang et al., Ionic conduction in polymer-based solid electrolytes. Adv. Sci. **10**, 2201718 (2023)
49. A. Nag, M.A. Ali, A. Singh, R. Vedarajan, N. Matsumi, T. Kaneko, N-Boronated polybenzimidazole for composite electrolyte design of highly ion conducting pseudo solid-state ion gel electrolytes with a high Li-transference number. J. Mater. Chem. A **7**, 4459–4468 (2019)

50. K. Zhang, Q. He, F. Xiong, J. Zhou, Y. Zhao, L. Mai et al., Active sites enriched hard carbon porous nanobelts for stable and high-capacity potassium-ion storage. Nano Energy **77**, 105018 (2020)
51. B.P. Vinayan, H. Euchner, Z. Zhao-Karger, M.A. Cambaz, Z. Li, T. Diemant et al., Insights into the electrochemical processes of rechargeable magnesium–sulfur batteries with a new cathode design. J. Mater. Chem. A **7**, 25490–25502 (2019)
52. J. Lee, W. Choi, Surface modification of sulfur cathodes with PEDOT: PSS conducting polymer in lithium-sulfur batteries. J. Electrochem. Soc. **162**, A935 (2015)
53. P. Rajkumar, K. Diwakar, R. Subadevi, and M. Sivakumar, "Preparation and Physical Characterization of sulfur/Carbon Black Composite Cathode Material for Li-s battery," *Int. Res. J. Eng. Technol.(IRJET),* 3, 2017.
54. C.C. Zuluaga-Gómez, C.O. Plaza-Rivera, B. Tripathi, R.K. Katiyar, D.K. Pradhan, G. Morell et al., Holey graphene/ferroelectric/sulfur composite cathodes for high-capacity lithium-sulfur batteries. ACS Omega **8**, 13097–13108 (2023)
55. N.D. Shcherban, S.M. Filonenko, P.S. Yaremov, S.A. Sergiienko, V.G. Ilyin, D.Y. Murzin, Carbothermal synthesis of porous silicon carbide using mesoporous silicas. J. Mater. Sci. **52**, 3917–3926 (2017)
56. H.M. Sajid, H. Afzal, M. Irfan, M. Saleem, R. Jan, S. Javed et al., Design of multilayered 2D nanomaterial composite structures for EMI shielding analysis. ACS Omega **7**, 35586–35594 (2022)
57. N. Radhakrishnan, C. Sobhan, Thermophysical characterization and melting heat transfer analysis of an organic phase change material dispersed with GNP-Ag hybrid nanoparticles. Heat Mass Transf. **58**, 1811–1828 (2022)
58. V.D. Mote, Y. Purushotham, B. Dole, Williamson-hall analysis in estimation of lattice strain in nanometer-sized ZnO particles. J. Theor. Appl. Phys. **6**, 1–8 (2012)
59. M.K. Alam, M.S. Hossain, N.M. Bahadur, S. Ahmed, A comparative study in estimating of crystallite sizes of synthesized and natural hydroxyapatites using scherrer method, Williamson-Hall model, Size-strain plot and halder-wagner method. J. Mol. Struct. **1306**, 137820 (2024)
60. R. Gamal, S.I. Elkalashy, E. Sheha, M. El Kholy, Polymer electrolytes based on magnesium triflate for quasi-solid-state magnesium-sulfur batteries. Phys. Scr. **97**, 065816 (2022)
61. R. Agrawal, D.K. Sahu, Y. Mahipal, R. Ashrafi, Investigations on ion transport properties of hot-press cast magnesium ion conducting nano-composite polymer electrolyte (NCPE) films: effect of filler particle dispersal on room temperature conductivity. Mater. Chem. Phys. **139**, 410–415 (2013)
62. A.S.N.B. Ismadi, N.K.B. Jaafar, M.Z.B.M. Yusoff, Structure and electrical properties of polymer electrolyte based on plasticized chitosan grafted polymethyl methacrylate (Ch-g-PMMA)-magnesium triflate for electrochemical double layer capacitor. Trends Sci. **21**, 7317–7317 (2024)
63. A. Rosdi, N. Zainol, and Z. Osman, "Ionic transport and electrochemical stability of PVDF-HFP based gel polymer electrolytes," in *AIP Conference Proceedings*, 2016.
64. J. Sharma, S. Hashmi, Plastic crystal-incorporated magnesium ion conducting gel polymer electrolyte for battery application. Bull. Mater. Sci. **41**, 1–8 (2018)
65. J. Sharma, S. Hashmi, Magnesium ion-conducting gel polymer electrolyte nanocomposites: effect of active and passive nanofillers. Polym. Compos. **40**, 1295–1306 (2019)
66. W. Ren, D. Wu, Y. NuLi, D. Zhang, Y. Yang, Y. Wang et al., An efficient bulky Mg [B (Otfe) 4] 2 electrolyte and its derivatively general design strategy for rechargeable magnesium batteries. ACS Energy Lett. **6**, 3212–3220 (2021)
67. S. Chen, Y. Wang, Y. Sun, D. Zhang, S. Zhang, Y. Zhao et al., Research status and prospect of separators for magnesium-sulfur batteries. J. Energy Chem. **87**, 225 (2023)